Ultra Fast Current Shunt (UFCS): A Gigahertz Bandwidth Ultra Low Inductance Current Sensor

Luke Shillaber, Yunlei Jiang, *Student Member*, IEEE, Li Ran, *Senior Member*, IEEE, Teng Long, *Member*, IEEE

***Abstract*—In an effort to reduce switching loss, increase switching frequencies and shrink passive component sizes, power device switching times are being pushed into nanosecond and sub-nanosecond intervals. However these fast switching times require high rates of change of current making the power devices susceptible to over-voltage damage from parasitic inductance in the power loop. This presents challenges in measuring the device switching current accurately and in turn makes accurate measurements of device switching energy and stored charge difficult. Traditional current measurement methods either do not have the required frequency response to view the switching edge accurately or have a high parasitic inductance that can significantly alter switching performance and cause damage to the power device. In this paper an active current measurement system is developed. This circuit achieves up to 1.6 GHz bandwidth with zero overshoot. By utilizing mutual inductance cancellation an insertion inductance down to 20 pH has been achieved. The research performed in this paper thereby allows for accurate measurement of device switching loss with minimal power circuit disturbance. The performance of this current measurement is experimentally verified in the frequency domain using a vector network analyzer (VNA) and time domain switching measurements are compared with state of the art current measurement.**

I. Introduction

Many factors of a power converter are heavily dependent on semiconductor device switching performance. Switching speed is being pushed faster in order to reduce switching loss, increase switching frequencies and improve power density.

Wide bandgap devices, most notably those made of GaN and SiC, are facilitating this increased speed. The low capacitance of these devices allows for high switching speeds with sub 10 ns current edges being achieved in power applications [1], [3]. In order to accurately measure switching loss and view the switching behavior of the device, complimentary high-bandwidth current measurement systems are required.

Assuming a measurement system with one dominant real pole, the 10%-90% rise time t_{rise} of a measurement probe is related to its bandwidth through the following equation:

$$f_{3dB} = \frac{\ln(9)}{2\pi t_{rise}} \approx \frac{0.35}{t_{rise}} \tag{1}$$

Manuscript received Month xx, 2021;revised Month xx 2022; Month xx 2022. *(Corresponding author: Teng Long).*

This work made use of the facilities at the Department of Engineering - Electrical Engineering Division, University of Cambridge, Cambridgeshire, CB3 0FA, U.K.

Luke Shillaber, Yunlei Jiang and Teng Long are with the Department of Engineering - Electrical Engineering Division, University of Cambridge, Cambridgeshire, CB3 0FA, U.K. (e-mail: ls669@cam.ac.uk, yj306@cam.ac.uk, tl322@cam.ac.uk).

Li Ran is with the School of Engineering, University of Warwick, Coventry, CV4 7AL, U.K. (e-mail: l.ran@warwick.ac.uk).

Additionally, the total rise time ($t_{rise,t}$) of a cascaded system is given in [6] as:

$$t_{rise,t} = \sqrt{t_{rise,1}^2 + t_{rise,2}^2 + ... + t_{rise,n}^2} \tag{2}$$

Through the use of (2) current measurement systems consisting of multiple poles can be analyzed by considering them as cascaded single-pole systems.

Using these equations we find that a typical commercial current measurement probe rise time of 12.5 ns (PEM CWT-Mini50HF) can only measure an edge of 27.3 ns with a 10% rise time error. An even higher bandwidth would be required to see the details of this edge and measure the switching loss accurately. This problem has been further investigated in [13] with modeling of the switching edge. It is also required that the system is well damped, inadequate damping of the measurement probe will cause measured overshoot and ringing that is not present in the real current. This can lead to inaccurate estimations of circuit board parasitic inductance/capacitance and introduces error and uncertainty into calculations involving charge transfer.

To achieve high switching speeds, power devices undergo high rates of change of current with 17.9 A/ns being reported in [1]. In accordance with these high rates of change, small inductances in the circuit have the potential to cause large voltage overshoots, in turn damaging the power device. In an effort to combat this issue and further increase switching speeds many low inductance power module designs have been proposed [1], [3], [7], [14], [12]. Whilst these address the issues of inductance in the power module, the inductance of available current measurement systems is not insignificant. For example, a typical coaxial shunt has an inductance of 6.5 nH, if this were to experience 17.9 A/ns there would be 116 V of overshoot. This has the potential to cause irreversible over-voltage damage to the power device. In addition to voltage spikes, high inductances within the circuit promote resonance and ringing of real currents within the power loop.

As wide-bandgap technology continues to mature the maximum device switching speed continues to increase with package inductances continuing to decrease. In consequence, measurement bandwidth requirements carry on increasing with maximum permissible inductances decreasing. Currently no single current measurement solution exists that will meet all present Wide-bandgap power semiconductor requirements, let alone those of future device technologies.

In this paper two resistive current probes are proposed. A power loop embedded current probe that achieves as low as 20 pH insertion inductance and an insertable current probe that

This article has been accepted for publication in IEEE Transactions on Power Electronics. This is the author's version which has not been fully edited and content may change prior to final publication. Citation information: DOI 10.1109/TPEL.2022.3184638

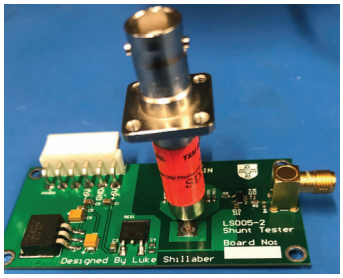

Figure 1: T&M SDN-414-10 Coaxial Current Shunt

achieves 260 pH insertion inductance. Compensation filters are developed in Section III-B. to extend the probe bandwidth to be in excess of 1.4 GHz whilst removing unwanted derivative components from the output signal. Frequency domain investigations are performed to determine the effects of the compensation filter and the probe bandwidth on the time domain response. A novel new Probe-to-PCB connection method is proposed in III-D. to allow the probe to be connected to existing power modules. This interconnect is designed with a low insertion inductance and small PCB footprint that is compatible with existing coaxial current shunts. Frequency and time domain tests are performed in Section IV. to verify the performance of both probes. These tests indicate a measured switching energy difference of up to 35% when compared with a state of the art commercially available coaxial current shunt. This is due to the uncompensated nature and high insertion inductance of such coaxial shunts.

II. Review of Existing Technology

Many current measurement systems are commercially available with differing advantages and drawbacks. Furthermore several measurement systems have been proposed in research that overcome some of these drawbacks to improve performance. This section reviews the most common commercially available high bandwidth measurement systems as well as some novel new systems proposed in research.

A. Commercially Available Probes

1) Coaxial Shunts: Coaxial current shunts work by measuring the voltage drop across a resistor of known value. They have a band-pass bandwidth well into the GHz range and offer good measurement shielding due to an enclosed construction resulting in a low mutual inductance between the power and measurement loops. These types of shunt typically have a large insertion inductance which has the potential to generate semiconductor device damaging voltages and promotes power loop ringing. Furthermore a proportion of this inductance appears between the measurement terminals of the device introducing a zero into the frequency response transfer function. This zero causes a scaled derivative of the real current to be present in the output signal. To extend the 'flat' portion of the bandwidth, high bandwidth Coaxial current shunts have a large resistance in the tens or hundreds of milliohms.

Fig. 2 shows the frequency response of a typical coaxial current shunt recorded on a Tektronix TTR500 network analyzer.

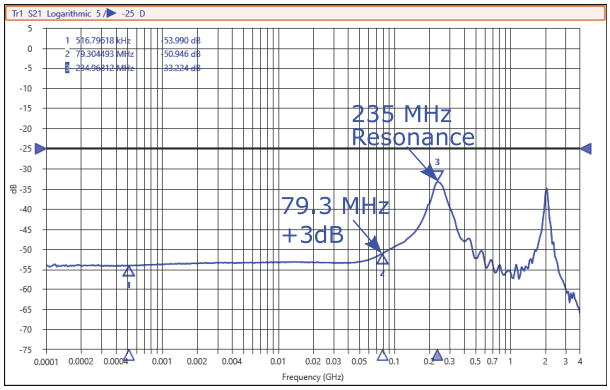

Figure 2: T&M SDN-414-10 Coaxial Current Shunt Frequency Response

To measure this frequency response the shunt was installed into a low 400 pH inductance power loop of approximately 67 pF parasitic capacitance, emulating a typical power module package. This shunt has a rated band-pass bandwidth of 2 GHz. By measuring this shunt we can determine an insertion inductance of approximately 6.5 nH. The differentiator type response limits the ±3 dB probe bandwidth to only 79.3 MHz with resonant peaks at 235 MHz and 2 GHz. The 235 MHz resonant peak is caused by the interaction of the current shunt inductance with the capacitance and inductance of the power loop. This is an indication of real resonant currents in the power-loop that will change in frequency and magnitude once the current shunt is removed. The research performed in [15] tests multiple coaxial current shunts indicating similar results, this paper also finds significant bandwidth differences between coaxial current shunts of the same model.

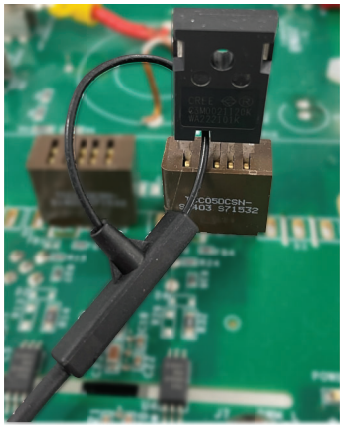

Figure 3: A PEM CWT Series Rogowski Coil

2) Rogowski Coils: Rogowski coils are magnetic measurement methods utilizing the principle of magnetic induction. As such they offer Galvanic isolation between the power and measurement circuits allowing for simultaneous measurements on both the high and low sides of the power loop. Due to this reliance on induction, Rogowski coils are unable to measure DC currents and thus a separate low bandwidth measurement system (for example a hall effect probe) is required to monitor DC parameters such as transistor on-state loss. Commercial

Rogowski coils require a primary measurement loop to be present in the power circuit. If no suitable loop is inherently present (e.g. a component leg) then a loop has to be added, increasing power circuit inductance by an amount dependent on the loop size. Furthermore, Rogowski coils require an output integrator to convert the induced voltage in the coil into a current measurement. The high frequency performance of the Rogowski coil is limited by the performance of the integrator and the turn-to-turn capacitance of the coil itself. For example, the state of the art PEM CWTMini50HF Rogowski coil achieves a bandwidth of 50 MHz. Rogowski coils can also experience measurement error due to voltage coupling through the capacitance between the coil and the circuit under test [2].

B. Current Measurement In Research

1) The Infinity Sensor: The infinity sensor [10] is a type of planar Rogowski coil that is placed over a trace within the PCB power loop. The fact that it can be placed over a power loop trace results in a very low insertion inductance of only 200 pH. The simulated bandwidth of the infinity sensor is quoted at 225 MHz, suggesting a significant improvement over conventional Rogowski coils. The frequency response and time domain switching data of the infinity sensor is not provided in the paper.

2) Integrated Current Measurement Coil: In [11] a current measurement coil is developed that is integrated into the power PCB layer stack-up. This scheme uses inductive coupling between the power loop and the integrated coil to achieve current measurement. Mathematical corrections are placed on the output circuit of the coil to remove any offset voltages. As the coil is integrated within the PCB it can have a very small effect on power loop inductance with GaN power loops of 0.33 nH inductance being reported. However, as the coil forms a trace on the PCB it could potentially limit the PCB layout possibilities and could not be implemented into "pre-made" power circuits. The bandwidth of the measurement circuit has not been directly measured but the time domain performance matches well with coaxial current shunt measurements.

3) Compensated SMD Current Shunts: SMD current shunts utilize multiple parallel SMD resistors to achieve a low inductance, low resistance current shunt. Unfortunately, not all of the inductance can be removed from the shunt resistors and thus a zero will remain in the frequency response and derivative components will be present in the output signal. A number of methods have been proposed to overcome this. In [5] a passive low pass filter is used to compensate for the zero. This gives the potential for a very large bandwidth but with very little gain and susceptibility to output loading effects. In [8] an undisclosed filter is used, with additional amplification using differential amplifiers in order to increase the output signal level. The bandwidth of this circuit is, however, restricted to 150 MHz due to limitations of the amplifiers. The current shunt resistors also have to be integrated into the power module at the design stage.

4) SMD Coaxial Current Shunts: In [16], [4] SMD resistor based Coaxial current shunts are proposed. The coaxial structure reduces the mutual inductance between the measurement and power loops to almost zero. The PCB structure utilizes multiple SMD resistors to keep the inductance between the measurement terminals extremely low. This grants the current shunt a large bandwidth without the need for a compensation filter. The coaxial shunt structure allows for a large canceling mutual inductance between the input and output currents, thereby reducing the total insertion inductance of the coaxial current shunt. To achieve a strong coaxial structure with good mutual inductance cancellation the resistors are placed vertically to form part of the shunt wall. This is in contrast to the traditional horizontal PCB solder placement of resistors. Fig. 4 shows the coaxial shunt design as reported in [16]. This design achieves an extremely high maximum bandwidth of 2.23 GHz and low minimum insertion inductance of 0.12-0.6 nH.

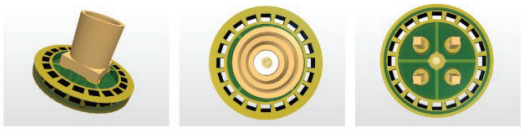

Figure 4: The SMD Coaxial Shunt Structure Proposed in [16]

The circular coaxial structure does not integrate well with traditional power module layout designs where the current is only coming from a single direction due to the center terminal of the shunt being completely obscured by the rest its body. This can make the design difficult to solder into the power loop whilst also causing the shunt to require significant PCB surface area.

The lack of zero compensation filter results in the bandwidth of the shunt being heavily dependent on shunt resistance, with lower shunt resistances having a lower bandwidth. In [16] the bandwidth of the shunt is reduced to 125 MHz for a 10 mΩ design. The large required resistance for high bandwidth can cause power dissipation issues when performing continuous measurements on high current signals. Furthermore, high bandwidth oscilloscopes have a significant range limitation, with a typical limitation of 10 V peak-peak at 50 Ω input impedance. This corresponds to 90 A peak-peak current limit when used with the high bandwidth 110 mΩ shunt proposed in [16]. High accuracy high bandwidth attenuators would be required to perform measurements of larger currents. The lack of compensation also results in a zero being present in the frequency response, although the bandwidth is high this zero still causes derivative distortion of the output signal.

C. Summary

Many current measurement systems have been proposed for wide-bandgap device testing. However, these have significantly limiting factors for wide-bandgap device measurement. These factors include, bandwidth, signal distortion, insertion inductance and device footprint. This is particularly pressing as switching edges tend towards sub 10 ns times, with no commercially available current probes being suitable for such a purpose. The probes mentioned in this section have been

This article has been accepted for publication in IEEE Transactions on Power Electronics. This is the author's version which has not been fully edited and content may change prior to final publication. Citation information: DOI 10.1109/TPEL.2022.3184638

summarized in Table I along with the UFCS systems proposed in this paper.

III. Basic Operating Principles of the Proposed Current Measurement System

The current measurement system proposed in this paper is based on the SMD shunt structure, building upon the research performed in [9] to improve versatility and system characterization. Compensation techniques have been developed in order to completely remove the parasitic zero from the frequency response and extend the probe bandwidth. The system can be embedded into the PCB power loop (UFCS-E) in order to eliminate interconnect parasitics, resulting in a frequency response with no peaking. Alternatively an insertable shunt (UFCS-I) has been proposed that can be soldered or clamped into a power loop or bus-bar for maximum versatility. Mutual inductance cancellation has been utilized in order to minimize the insertion inductance of both probes. Split measurement and power grounds are provided in order to reduce ground noise. The shunt construction can be characterized by 4 separate stages as shown in Fig. 5:

1) The shunt resistance is formed using SMD type construction. Mutual inductance cancellation is used to reduce the inductance of the shunt.
2) To remove the inevitable inductive zero of the shunt and to extend its bandwidth, a low pass filter (LPF) stage is realized.
3) The signal is then amplified and transported across the power PCB as a differential signal so as to reject noise.
4) The signal is further amplified and converted to a 50 Ohm impedance matched connection for measurement equipment such as an oscilloscope.

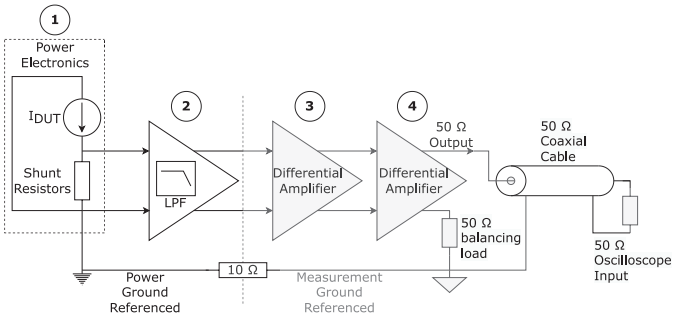

Figure 5: Outline of the Proposed Current Measurement System

A. The Shunt Resistor

The current measurement system designed in this paper is to use an SMD type current shunt structure. The layout of this structure can be seen in Fig. 6a. It is designed to use the mutual inductance between the current paths into and out of the current shunt to reduce the total loop inductance. The return path after the current shunt is placed on the layer directly under the resistor, furthermore a thin 100 um FR4 top layer thickness is used on the PCB to provide a large mutual inductance. The shunt resistors are placed face down

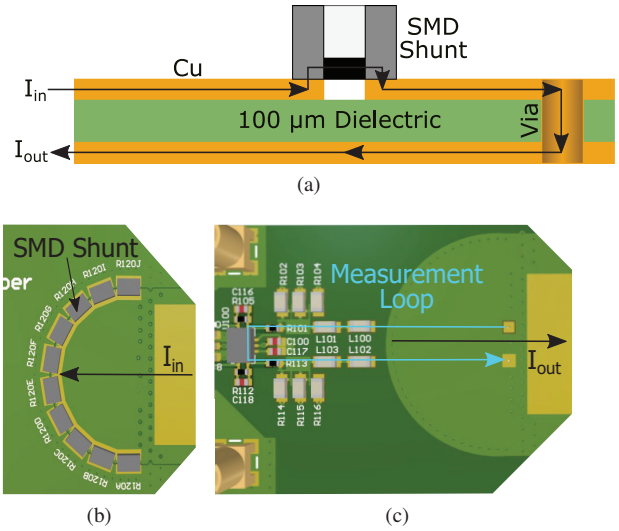

Figure 6: Design of the SMD Current Shunt (a) Layup of the Shunt Resistors (b) Top Side of Probe (c) Bottom Side of Probe

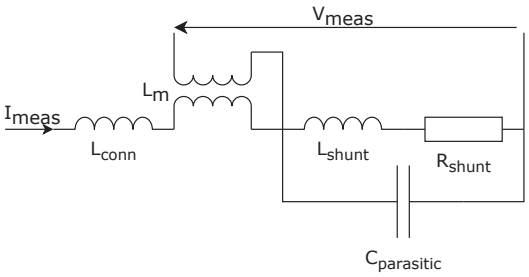

Figure 7: SMD Current Shunt Equivalent Circuit

as the conductive layer is on the top side of the resistor. By placing the resistor face down a larger mutual inductance can be had between the resistor and the current return path, thereby reducing the total loop inductance.

The shunt resistors are placed onto the PCB in a semi-circular arrangement as shown in Fig. 6b with the voltage measurement point placed at the center of the semicircle. This reduces the required PCB trace width for a given number of resistors and consequently the spacial requirements of the shunt. The use of separate resistors reduces the skin effect, with the spaced and angled resistors avoiding the proximity effect. The shunt is formed using 10 of 0508 current shunt resistors. The 0508 package is a short wide package, available in small sizes of fine tolerance (<100 mΩ, 0.1%) and has a high maximum power dissipation of 0.667 W. A coaxial connector is placed at the center of the shunt to allow for the frequency response of the circuit to be tested and the shunt inductance measured.

The proposed shunt design can be modeled by the equivalent circuit shown in Fig. 7.

This leads to the following transfer function $G_0(s) = V_{meas}/I_{meas}$:

Probe	Type	Quoted Bandwidth (MHz)	Insertion Inductance (nH)	Measurement Rise Time (ns)	DC Capable
T&M SDN-414-10	Coaxial Shunt	2000	5-7**	0.18	Yes
PEM CWTMini50HF	Rogowski Coil	50	Application Dependent	12.5	No
University of Bristol Infinity Sensor [10]	Rogowski Coil	225	0.2	1.56*	No
Dresden University of Technology SMD Shunt [5]	SMD Shunt	Not Given	<0.5	N/A	Yes
Integrated Current Measurement [11]	Pick-Up Coil	Not Given	<0.33	N/A	No
Cambridge University Compensated Shunt [8]	SMD Shunt	150	<0.6	2.33*	Yes
Surface Mount Coaxial Shunt Resistor [16]	SMD Shunt	Up to 2230***	0.12	Not Given	Yes
Cambridge Ultra Fast Current Shunt Embedded (UFCS-E) (this work)	SMD Shunt	1550	~0.02, Power Loop Layer Stack Dependent	0.355	Yes
Cambridge Ultra Fast Current Shunt Insertable (UFCS-I) (this work)	SMD Shunt	1480	0.26	0.355	Yes

*Calculated assuming a flat bandwidth with single pole roll off.
**Dependent on length of PCB mounting leads.
***Dependent on resistance.

Table I: Comparison of Current Measurement Probes

$$G_0(s) = \frac{R_{shunt} + s(L_{shunt} + L_m)}{s^2 L_{shunt} C_{parasitic} + s R_{shunt} C_{parasitic} + 1} \quad (3)$$

where $s = j\omega$

L_{shunt} is the inductance of the shunt circuit between the current measurement points. L_m is the mutual inductance between the power and measurement loops, this is minimized in the shunt design by keeping the power and measurement loops perpendicular as shown in Fig. 6c. R_{shunt} is the resistance of the measurement circuit between the measurement points, this is dominated by the shunt resistance. $C_{parasitic}$ is the equivalent parasitic capacitance that appears across the shunt resistor, bypassing it. This is composed of components from both the shunt circuit and the system under test. In low inductance applications the capacitance is predominantly through the PCB due to the close layer spacing required for effective mutual inductance cancellation. L_{conn} is the extra inductance introduced into the power-loop, external to the shunt, due to its interconnect. If the shunt is integrated directly into the power-loop, then L_{conn} is zero. From (3) we can determine that the natural frequency of the shunt is $1/\sqrt{L_{shunt} C_{parasitic}}$ and the damping ratio of the shunt is $\frac{R}{2}\sqrt{\frac{C_{parasitic}}{L_{shunt}}}$, this clearly indicates that by keeping the shunt inductance L_{shunt} as small as possible we do not only protect the device from voltage spikes, but also increase the damping ratio of the current shunt and increase its natural frequency away from the frequencies of interest.

B. The Filter

From (3) we can see that, as for any resistive type shunt, there is an inductive zero introduced by the shunt at the position $\omega = R_{shunt}/(L_{shunt} + L_m)$. Rearranging (3):

$$V_{meas}(s) = \frac{(1 + \frac{s(L_{shunt}+L_m)}{R_{shunt}}) R_{shunt} I_{meas}}{s^2 L_{shunt} C_{parasitic} + s R_{shunt} C_{parasitic} + 1} = (1 + \frac{s(L_{shunt} + L_m)}{R_{shunt}}) F(s) \quad (4)$$

Taking an inverse Laplace transform of this system we achieve (where $f(t) = \mathcal{L}^{-1}(F(s))$):

$$V_{meas}(t) = f(t) + \frac{(L_{shunt} + L_m)}{R_{shunt}} \dot{f(t)} \quad (5)$$

Thus the presence of the inductive zero adds derivative components into the output measured signal. Due to the high speed nature of a semiconductor switching edge the derivative component can be very large, ruining the accuracy of the measured signal.

To remove this zero, the voltage across the shunt is passed through a differential low-pass filter. The filter used is formed from an inductive filter utilizing high bandwidth SMD chip-type inductors and the input impedance of a differential amplifier stage. The construction of this filter can be seen in Fig. 9. Given this design we have two degrees of freedom for altering the pole positions of the filter - both the resistance R_3 and the inductance L_{comp} can be changed in order to finely tune the filter frequency response. It is vital that this filter is tuned as accurately as possible. The effects of compensation error can be seen in the LT Spice simulations of Fig. 8. Fig. 8a shows the frequency responses of typical under and over compensated UFCS probes, Fig. 8b shows the corresponding switching current measurements of those probes when used in a 52 A double pulse test of a Wolfspeed CPM2-1200-0025B SiC power device. From these waveforms we can clearly see the effects of compensation error, with 1.5 dB over compensation causing a false tail current of 4.5 A magnitude.

It is imperative that the parasitic inductive reactance of R_3 does not approach its resistance so as not to distort the frequency response of the filter. As such R_3 is formed from three separate 0603 SMD resistors. It should be noted that high bandwidth differential amplifiers require very specific feedback resistances in order to achieve the maximum bandwidth specified in the data-sheet. Due to this a capacitive feedback low pass filter is not feasible as only the capacitor size would be variable with a very limited range of available values.

This article has been accepted for publication in IEEE Transactions on Power Electronics. This is the author's version which has not been fully edited and content may change prior to final publication. Citation information: DOI 10.1109/TPEL.2022.3184638

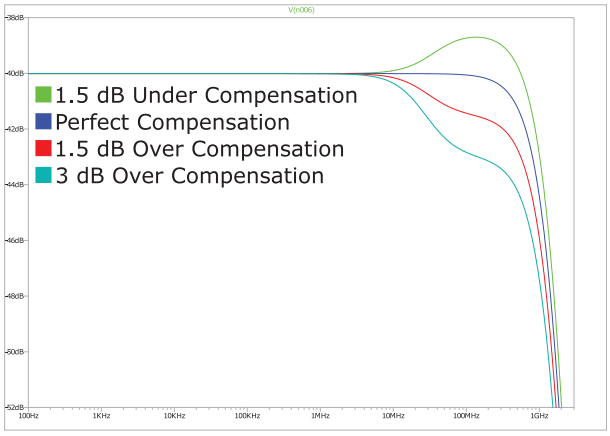

(a)

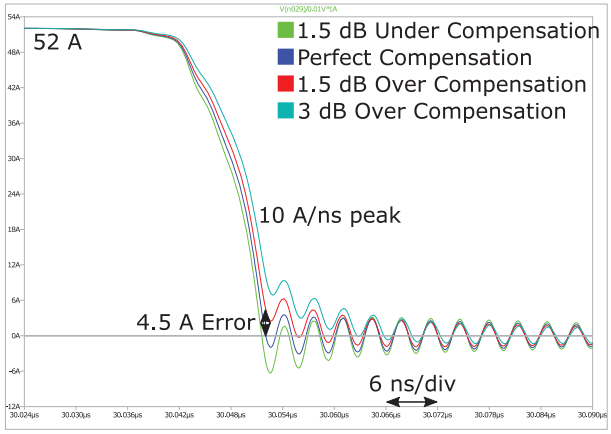

(b)

Figure 8: The Effects of Compensation Error on a 33 MHz Zero (a) In the Frequency Domain (b) In the Time Domain

By having a differential amplifier at the output of the filter, the unbalanced differential signal at the output of the inductor is converted into a balanced differential signal allowing the later removal of common mode noise. After the differential filter, the circuit transfer function can be represented by (6) where A_1 is the response of the differential amplifier - typically a low pass filter with constant gain within its bandwidth. Consequently, as long as L_{shunt} and $C_{parasitic}$ are kept sufficiently small that resonant effects to not occur within the frequencies of interest, the shunt frequency response will be dominated by the response of the differential amplifiers.

$$G_1(s) = \frac{A_1 R_{shunt}}{-\omega^2 L_{shunt} C_{parasitic} + j\omega R_{shunt} C_{parasitic} + 1} \quad (6)$$

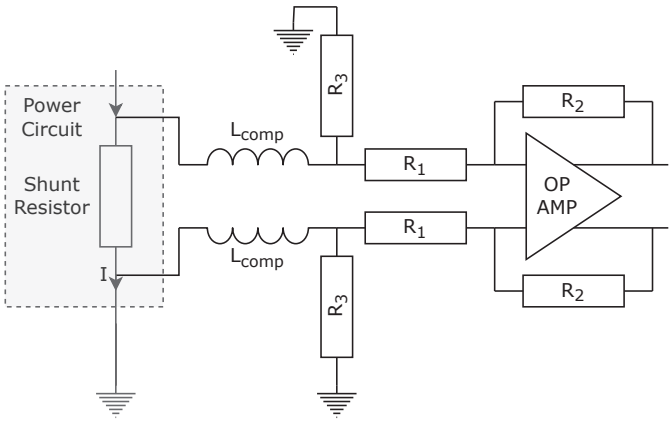

Figure 9: Current Measurement Compensation Filter

C. Amplification and Output Conversion

The balanced differential signal is then passed over a split between analog and digital grounds separated by a 10 Ω resistance. This split in the ground plane discourages any power ground currents from flowing into the sensitive measurement circuitry and equipment. The power ground currents have the potential to be quite large and contain significant high frequency content. These currents thereby have the ability to significantly corrupt measurement signals. The grounding of the power supplies is also critical. To remove the need for isolated power supplies a star grounding technique is adopted with common mode chokes being placed between different ground references.

The differential signal is further amplified before being converted into a single ended signal for connection to an oscilloscope. This is again achieved using a differential amplifier by utilizing just one output leg. The other leg is loaded by an equivalent 50 Ω impedance so that the two differential lines remain symmetrical, this will maximize the common mode rejection ratio (CMRR) of the amplifier. A conventional differential input single ended output amplifier was not used for this purpose as the bandwidth on one input is often significantly less than the other.

The addition of the amplification stages has a further advantage of buffering the current shunt from the oscilloscope input, with the resistors in the amplifier feedback loops blocking any direct connection. If there were to be a failure that caused high voltage to be present across the current shunt resistor, for example if the shunt resistor were to fail open circuit, then the amplifier circuits will be the first components to experience this high voltage thereby providing some protection to the oscilloscope input.

As the amplifier frequency response is part of the full system bandwidth it is clearly important that amplifiers with a wide bandwidth are selected for use throughout the signal path. The bandwidth of these amplifiers should be much greater than the required bandwidth of the probe due to the compounding of amplifier roll-off and equivalently through (1) the compounding of rise time as given by (2). Furthermore any distortion that these amplifiers introduce will distort the output signal, amplifiers are available that can be configured to

This article has been accepted for publication in IEEE Transactions on Power Electronics. This is the author's version which has not been fully edited and content may change prior to final publication. Citation information: DOI 10.1109/TPEL.2022.3184638

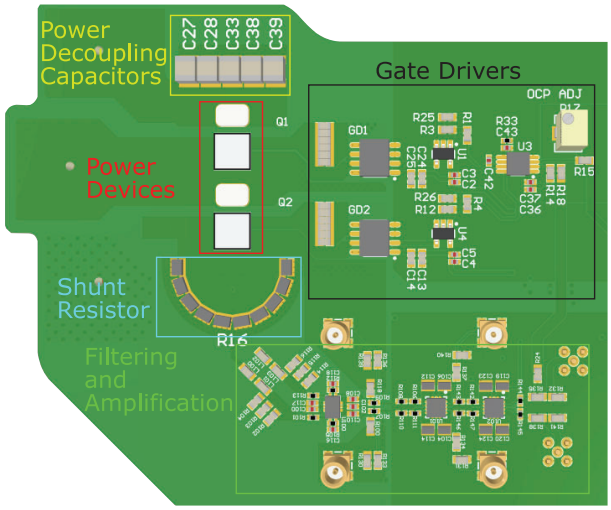

Figure 10: UFCS-E Implementation Example

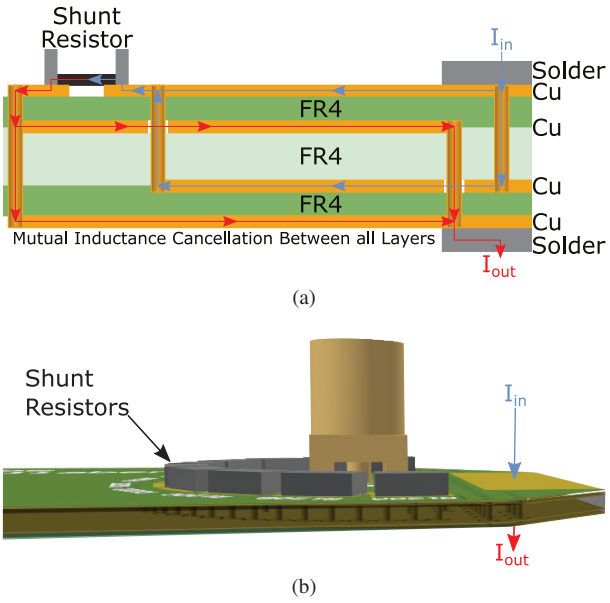

Figure 11: Current Paths Within the UFCS-I (a) Multi-Loop Interconnect Design (b) Physical Shunt Implementation

introduce no overshoot, these should be used for all amplifiers in the signal path. Due to the high measurement bandwidth input noise of the measuring oscilloscope is high. Therefore, in order to maximize the signal to noise ratio an amplifier with a large output voltage should be selected.

D. Embedded and Insertable Construction

To minimize the interconnect parasitics of this circuit it is best to embed the shunt resistors into the power loop (UFCS-E) as shown in Fig. 10. This has the disadvantage that the current measurement has to be included at the power module design stage and may not be compatible with the power module PCB layer stack-up or may be unsuitable for layouts with a high component density.

To combat this an insertable current shunt is proposed (UFCS-I). To make the shunt as versatile as possible whilst maintaining a low insertion inductance, a multi-loop PCB interconnect has been developed as depicted in Fig. 11a. This connection method is designed so as to utilize mutual inductance cancellation between multiple PCB layers, whilst still allowing for the mechanical strength advantages of a thick PCB. Using Ansys Q3D extractor it was found that this four layer construction gives a 47% inductance reduction over a traditional two layer loop of the same 0.8 mm PCB thickness. Furthermore, the connection has been developed so as to be compatible with traditional through hole current shunts and consequently is compatible with existing designs such as the the GaN systems GS66508T-EVBDB2 development board as demonstrated in Fig. 12a. The thin profile of this connection method also allows it to be connected into bus-bars with minimal circuit disturbance, this can be seen in Fig. 12b.

Due to the high frequency content of the measured signals it is vital that good RF design techniques are adhered to. The PCB material used in the construction of both current probes is an FR4 material with a relative permittivity $\varepsilon_r = 4.05$, consequently the minimum wavelength (λ_{min}) of the measured signal on this PCB is 149 mm at 1.4 GHz. As long as the spacings between the shunt resistor and consecutive amplifier

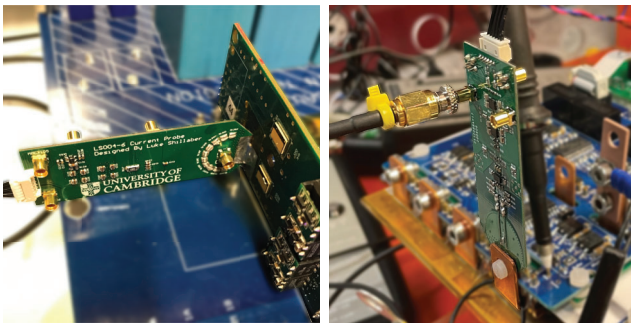

(a) (b)

Figure 12: UFCS-I Use Configurations (a) Solder Connection (b) Bus-bar Connection

stages on the measurement circuit are much lower than this wavelength then standard PCB design procedures may be used and impedance matching is not necessary. For the construction of the UFCS current measurement shunts a design requirement of <15mm between amplifier stages was used. Consequently impedance matching is only necessary for the oscilloscope output connection. UFCS-E embedded shunt designs on power modules of alternative PCB dielectrics are possible as long as this design criterion is adhered to.

IV. Experimental Results and Calibration.

A. Inductance measurement and Filter Calibration

In order to correctly design the zero compensation filter, the position of the parasitic zero must be determined. This can be achieved by using a Vector Network Analyzer (VNA). Fig. 13 shows the VNA connection schemes for both the embedded and insertable current probes. A 50 Ω resistor is placed in series with the shunt resistance in order to create an impedance matched connection to the VNA. As the power loop is not

This article has been accepted for publication in IEEE Transactions on Power Electronics. This is the author's version which has not been fully edited and content may change prior to final publication. Citation information: DOI 10.1109/TPEL.2022.3184638

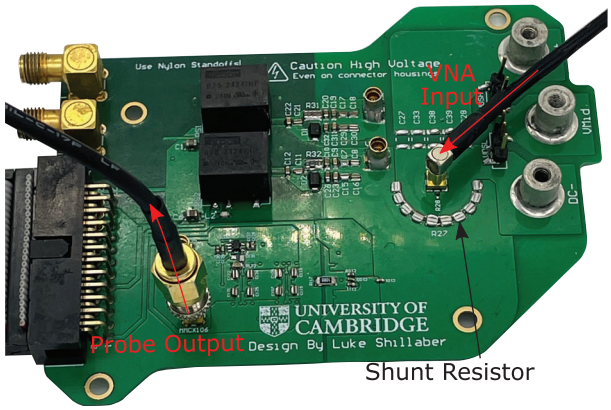

(a)

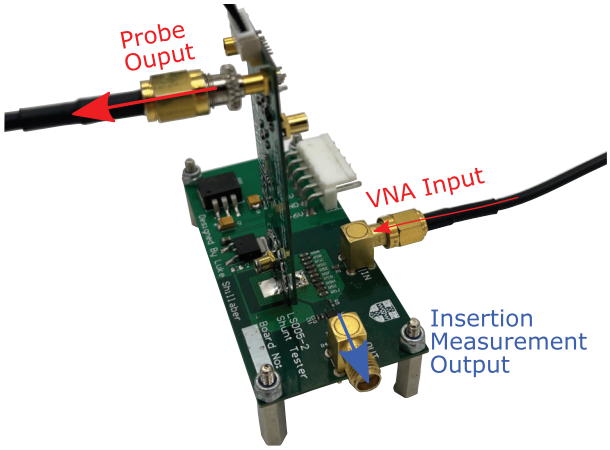

(b)

Figure 13: VNA Connections of the UFCS Current Probes (a) UFCS-E Measurement (b) UFCS-I Measurement

impedance matched, the resistor is placed as close as possible the current shunt resistor to minimize RF reflections within the frequencies of interest. The resistor is also placed central to the power loop feeding the current shunt so as to give an equal impedance to each shunt resistor and replicate the real power loop current. When performing frequency response measurements it is best to remove power devices, decoupling capacitors and wire connections from the power loop as these will lead to increased RF reflections that will appear in the measured result.

Fig. 14 shows the uncompensated frequency response of a typical UFCS-E embedded current measurement circuit with a total shunt resistance of 10 mΩ. This plot has a clear 20 dB/decade rise at high frequencies, continuing up to the bandwidth of the differential amplifiers used. This corresponds well with the theory of a single zero caused by the effective inductance $L_{shunt} + L_m$. The +3dB frequency rise can be seen to be at 135 MHz indicating a total effective inductance of 12 pH. The inductances L_{shunt} and L_m are both heavily dependent on the PCB layer stack used. As the embedded shunt forms part of the power module layer stack the inductances will scale accordingly with the power module design. For the 0.1 mm PCB layer separation used in this paper the total loop inductance of the test circuit, excluding switching

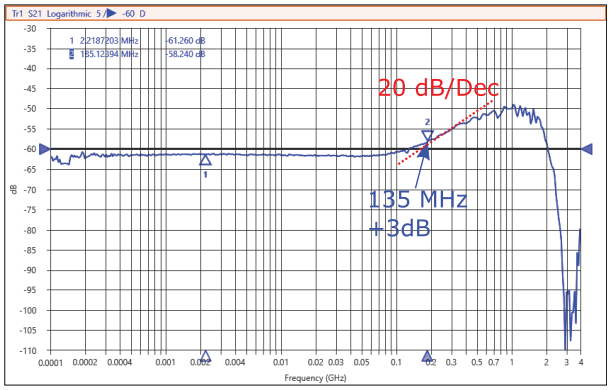

Figure 14: UFCS-E Uncompensated Frequency Response

devices, is simulated using Ansys Q3D to be 410 pH. The mutual inductance L_m between the power and measurement loops is simulated to be -8 pH at 135 MHz, indicating a total shunt resistor insertion inductance of 20 pH. This is much lower than the total power loop inductance and thus will have a negligible effect on power module performance.

Now that the shunt zero position is known the compensation filter can be calibrated using the following equation:

$$L_{comp} = \frac{R_1 R_{in}}{2\pi f_{3dB}(R_1 + R_{in})} \tag{7}$$

Where R_{in} is the input impedance of the amplifier stage:

$$R_{in} \approx \frac{2R_1(R_1 + R_2)}{2R_1 + R_2}\Bigg| R_3 << R_1 \tag{8}$$

To calculate the values of L_{comp} and R_3 for this filter we first assume a value of R_3 such that R_{shunt}<<R_3<<R_1. This ensures that the filter does not conduct significant power loop current, whilst also making sure that it does not disrupt the operation of the differential amplifier. For the differential amplifier used $R_1 = R_2 = 150\ \Omega$, consequently an R_3 value of 10 Ω is selected. From (7) and referring to Fig. 9 a compensation inductance L_{comp} of 11 nH is then calculated. If the calculated inductor value is not an available size then R_3 can be further adjusted to fine tune the filter -3dB point. The addition of this filter will not add any undesired poles and zeros into the frequency response of the measurement system as the inductance to resistance ratios of the shunt and the filter are equal.

To fully characterize the performance of the insertable current measurement system the inductance of the interconnect must also be measured. To measure this, the shunt is installed onto a test circuit as shown in Fig. 13b. This test circuit has a series resistance R_{PCB} of 100 mΩ and series Inductance L_{PCB} of 515 pH. These parameters appear in series with the current shunt and come together with the impedance matching resistances to form a potential divider as shown in Fig. 15. The frequency response of this potential divider can be analyzed to determine the probe insertion inductance.

Due to resonance between the UFCS-I probe and the test circuit capacitance, there is a resonant peak in the frequency response as shown in Fig. 16a. Looking at the +3dB point of

This article has been accepted for publication in IEEE Transactions on Power Electronics. This is the author's version which has not been fully edited and content may change prior to final publication. Citation information: DOI 10.1109/TPEL.2022.3184638

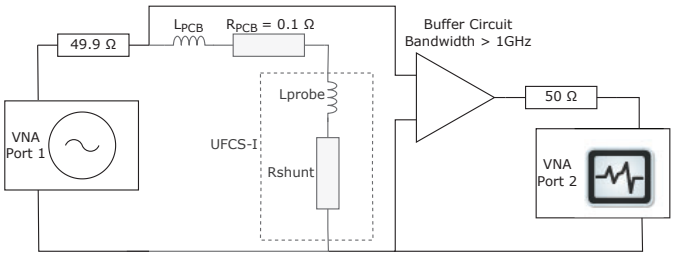

Figure 15: UFCS-I Insertion Inductance Measurement Equivalent Circuit

Fig. 16a, an estimate of the probe insertion inductance can be made:

$$L_{probe} = \frac{R_{PCB} + R_{shunt}}{2\pi f_{+3dB}} - L_{PCB} \tag{9}$$

This equation ignores the resonant effects of the probe, the +3dB point is in the linear region before the resonant peak and therefore the error from this simplification is small. Using (9) the measurement probe inductance ($L_{probe} = L_{conn} + L_{shunt}$) was calculated to be 260 pH. This is a significant improvement over commercially available high bandwidth current probes but nevertheless a higher inductance than the embedded UFCS-E design.

Calibrating the shunt in the same way as the UFCS-E embedded design yields the frequency response in Fig. 16b. With the +3dB frequency corresponding to a total zero inductance of 48 pH. This is slightly higher than the UFCS-E design due to the multiple return current paths in the multi-loop interconnect (as seen in Fig. 11a) having a weakened magnetic coupling to the current sense resistor.

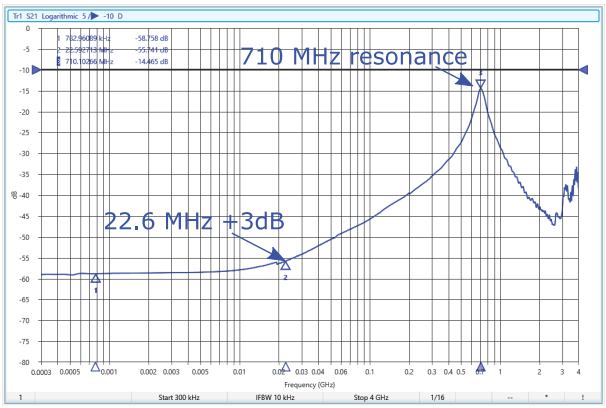

(a)

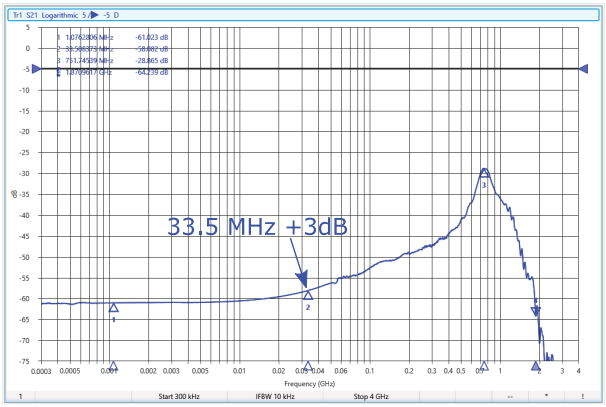

(b)

Figure 16: Uncompensated Insertable Shunt VNA Inductance Measurements (a) Insertion Inductance Measurement (b) Uncompensated Probe Frequency Response

B. Frequency response

Once the UFCS measurement system has been compensated a VNA can be used to test the full frequency response of the UFCS current probe designs, giving the results shown in Fig. 17a. From the derived second order frequency response of the circuit (6) we can see that the probe is expected to exhibit a form of damped resonance, the resonant frequency of this being:

$$\omega_d = \sqrt{\frac{4L_{shunt} - R_{shunt}^2 C_{parasitic}}{4L_{shunt}^2 C_{parasitic}}} \tag{10}$$

Taking the UFCS-E inductance of 20 pH, a shunt resistance of 10 mΩ and combining this with the 80 pF parasitic capacitance of a 50 A ultra low inductance power module gives a resonant frequency of around 3.98 GHz; this is well beyond the sharp roll-off of the operational amplifiers. Consequently the resonance of the probe will have negligible effect on the measured signal. Since the compensated shunt resistor has a flat frequency response within the bandwidth of the amplifier, the probe overshoot can be further analyzed by following the amplifier data-sheet. High bandwidth operational amplifiers are used that are configured to give zero overshoot and thus the current measurement probe can be considered to have zero overshoot.

For the insertable shunt design of higher 260 pH insertion inductance, 207 pF capacitance and 10 mΩ resistance when connected to a current shunt test circuit of 67 pF capacitance (found using Ansys Q3D extractor), 515 pH inductance and 100 mΩ resistance the operational bandwidth can be seen in Fig. 17b. Due to the parasitic capacitance of the test PCB a resonant peak is expected at approximately 698 MHz, this corresponds well with the 723 MHz peak seen in the VNA measurements. Whilst this peaking has the ability to cause resonance and overshoot in the output signal, it represents a resonance that will be present in the module under test. The peak of this resonance is also at a much higher frequency than other state of the art current shunts owing to the much lower parasitic inductance of the UFCS-E. The self resonant frequency of the UFCS-E current shunt between the measurement points is expected to be at 1.6 GHz, this is indicated in the measured frequency response of Fig. 17b by the small peak between the -3 dB and -12 dB points of the probe, whilst this peak causes a slight gain in the frequency response it is heavily attenuated by the roll-off of the operational amplifiers. Furthermore, the frequency of this peak is beyond the typical frequencies of interest in a switching edge and thus can be further attenuated through oscilloscope bandwidth limiting or data post-processing.

This article has been accepted for publication in IEEE Transactions on Power Electronics. This is the author's version which has not been fully edited and content may change prior to final publication. Citation information: DOI 10.1109/TPEL.2022.3184638

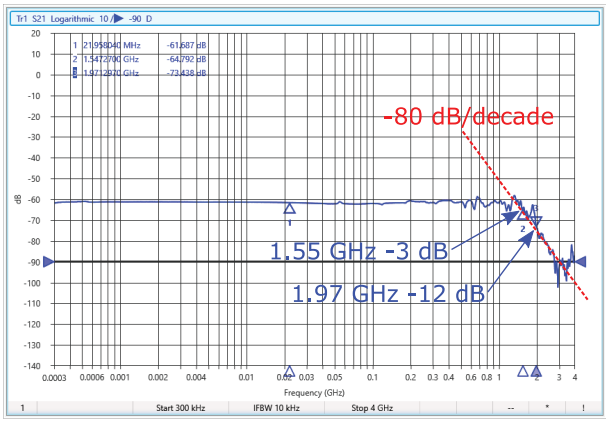

(a)

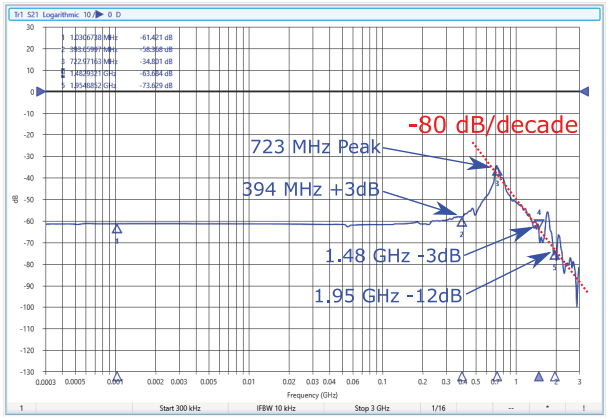

(b)

Figure 17: Current Shunt Frequency Responses (a) UFCS-E Embedded Shunt (b) UFCS-I Insertable Shunt

Assuming a probe damping ratio of 1 (4 repeating poles indicated by the 80 dB/decade roll-off) and taking the probe -12 dB point of 1.97 GHz (UFCS-E) the rise time of this measurement probe can be calculated using (1) and (2) to be 355 ps allowing a 1.11 ns edge to be measured with 5% rise time error.

It is difficult to make direct calculations of rise-time for the insertable shunt due to the resonance with the test PCB, all be it much reduced when compared with the higher inductance of available commercial current measurement alternatives. However, the compensation, layout and amplification design of the UFCS-I insertable shunt is exactly the same as the UFCS-E embedded shunt with the bandwidth being dominated by the operational amplifiers, consequently, the same rise time can be expected.

C. Time domain response,

To perform time domain tests both the UFCS-I insertable current shunt and a T&M SDN-414-10 coaxial current shunt were independently installed onto a GaN systems GS66508T-EVBDB2 half bridge module and double pulse tests performed.

The Turn-Off switching results can be seen in Fig. 18 and the Turn-On results in Fig. 19. In both figures the UFCS-I has the highest resonant frequency and much more heavily damped resonance, indicative of the much lower inductance of the probe. Typically resonance can make it difficult to correctly measure the switching energy of the device, with much of the transistor output capacitor (*Coss*) charge being contained within the resonance. Thus the UFCS-I makes switching energy measurement more accurate, simplifying the separation of conduction and switching energies. In Fig. 18b the voltage overshoot is reduced by 60.5 V and in Fig. 19b the voltage dip is reduced by 52 V due to the much reduced probe inductance. Comparing these inductive voltage spikes with rates of change of current ($\Delta V = L\frac{dI}{dt}$) the inductance difference can be calculated to be approximately 6 nH, coordinating well with the inductances measured using the VNA.

In Fig. 18a the UFCS-I indicates a longer current fall time and in Fig. 19a the UFCS-I indicates a longer current rise time (10%-90% DC Value) when compared to the coaxial current shunt. This is due to the combination of an increased damping ratio and lack of a parasitic zero in the frequency response of the UFCS probe. The derivative action of the zero in the Coaxial current shunt will cause a vertical shift in the measured current that is proportional to the rising/falling rate, thereby altering the rise time and causing current overshoot. The current overshoot is also contributed to by the resonance of the probe inductance with the power loop. From Table. II we can see that this has a very small effect on the turn-on switching energy, this is as the effects of the current overshoot are canceled by the effects of the inductive voltage drop. At turn-off, the voltage overshoot happens at very low current levels and as such does not have a significant canceling effect on the reduced switching energy due to the negative current overshoot. This results in the much reduced measured switching loss.

It can also be seen that in Fig. 18a and Fig. 19a there are notable glitches in the UFCS switching waveforms, this is input noise from the oscilloscope. The full-scale-range maximum output voltage of the amplifier used in the UFCS probe is 1.2 V. Due to the high bandwidth used for these measurements there is a high channel noise at the oscilloscope, this leads to the small glitches visible in the waveform. These glitches are reduced on the T&M SDN-414-10 due to its larger output voltage. If a lower speed measurement is being made, the bandwidth at the oscilloscope can be reduced to give a cleaner waveform. Furthermore for the UFCS-I it can be noticed that there is a significant secondary resonance imposed on the waveforms after the switching instance. Whilst this secondary resonance makes the waveforms appear unsmooth and noisy, it is a real resonance present within the circuit between the parasitic parameters of the circuit under test and the UFCS-I probe. This resonance is expected from Fig. 17b but is at a slightly different frequency (750 MHz rather than 723 MHz) due to the differing parasitics of the test circuits. The T&M SDN-414-10 does not undergo the same resonances due to its much high inductance reducing the resonant frequency and its much higher resistance increasing the damping effects.

Tests were also performed using the UFCS-E. To achieve this a new power module was constructed utilizing St-Microelectronics SiC die giving a low power loop inductance

This article has been accepted for publication in IEEE Transactions on Power Electronics. This is the author's version which has not been fully edited and content may change prior to final publication. Citation information: DOI 10.1109/TPEL.2022.3184638

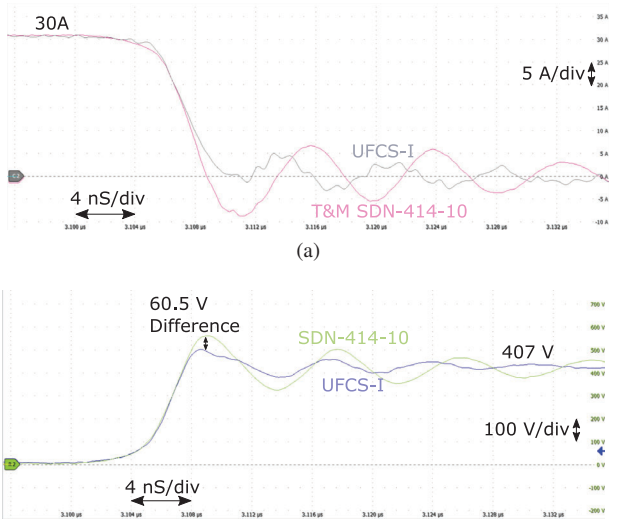

Figure 18: 30A Turn-Off Double Pulse Test Results recorded on a 2 GHz Tektronix MSO56 Oscilloscope (a) Current Comparison (b) Voltage Comparison

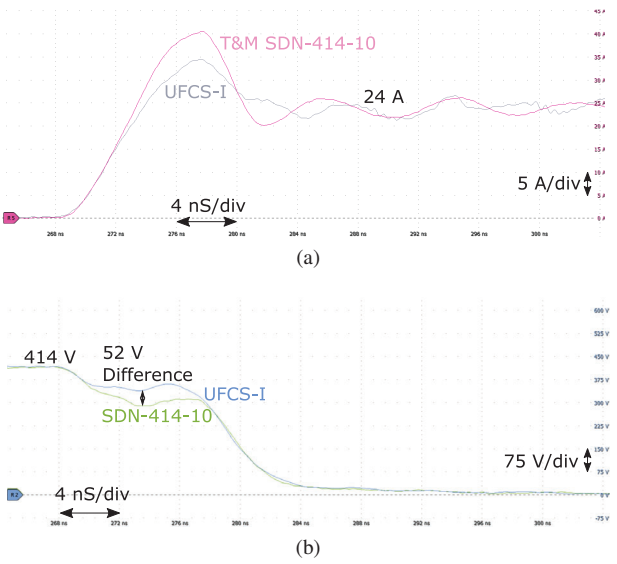

Figure 19: 24 A Turn-On Double Pulse Test Results recorded on a 1 GHz Tektronix MSO64 Oscilloscope (a) Current Comparison (b) Voltage Comparison

	Turn-Off		Turn-On	
Probe	**UFCS-I**	**SDN-414-10**	**UFCS-I**	**SDN-414-10**
Voltage rise/fall time (ns)*	3.4	3.3	13.7	13.1
Current rise/fall time (ns)*	3.7	3.4	4.0	3.5
Switching Energy (μJ)	26	17	90	91

*Calculated as 10-90% of DC value

Table II: Rise Time and Switching Energy Calculations

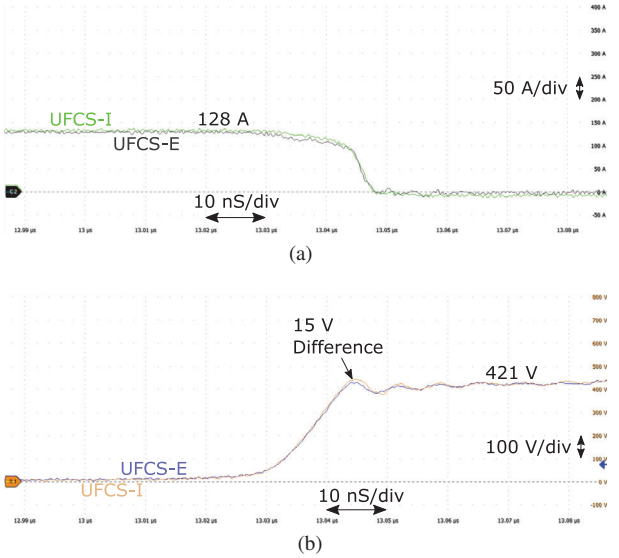

Figure 20: UFCS Probe Comparison 128 A Turn Off (a) Current Comparison (b) Voltage Comparison

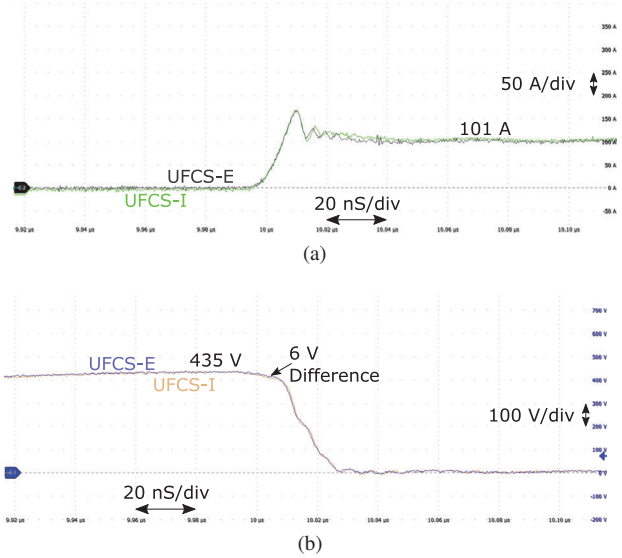

Figure 21: UFCS Probe Comparison 101 A Turn On (a) Current Comparison (b) Voltage Comparison

of 1 nH. Switching tests were performed using this module on both the UFCS-I and UFCS-E current measurement circuits independently. The T&M SDN-414-10 could not be used for this test as its through hole footprint is not compatible with the low inductance PCB design and its high insertion inductance could cause over-voltage damage to the Semiconductor Devices. The switching waveforms for these circuits can be seen in Fig. 20 and Fig. 21

From these waveforms it can be observed that there is an excellent agreement between the two measurement probes. The turn on voltage drop and turn off voltage overshoot for the UFCS-I is very slightly larger than that of the UFCS-E due to the 260 pH insertion inductance. A slight decrease in the resonant frequency after the switching instance can also be observed, again due to this inductance.

V. Conclusion

This paper has proposed two current measurement probes that achieve a very high -3dB bandwidth in excess of 1.4 GHz. An integrated current measurement probe has been proposed that achieves zero overshoot and 20 pH insertion inductance and an insertable current measurement probe has been proposed that achieves an insertion inductance of only 260 pH. A novel Multi Layer Interconnect has been realized for the insertable probe that can be constructed using traditional PCB design methods to allow for simple, non-intrusive connections into power loops and bus-bars. These probes have been tested in both the frequency and time domains indicating lower overshoot and resonance than a popular and readily available coaxial current shunt. This allows them to give easier and more accurate measurements of important parameters such as switching energy and transistor stored charge.

References

[1] Cai Chen, Zhizhao Huang, Lichuan Chen, Yifan Tan, Yong Kang, and Fang Luo. Flexible PCB-Based 3-D Integrated SiC Half-Bridge Power Module with Three-Sided Cooling Using Ultralow Inductive Hybrid Packaging Structure. *IEEE Transactions on Power Electronics*, 34(6):5579–5593, 2019.

[2] Chris Hewson and William F.Ray. The effect of electrostatic screening of Rogowski coils designed for wide-bandwidth current measurement in power electronic applications. *35th Annul IEEE Power Electronics Specialists Conference*, pages 1143–1148, 2004.

[3] Eckart Hoene, Andreas Ostmann, Binh The Lai, Christoph Marczok, Andreas Müsing, and Johann W. Kolar. Ultra-Low-Inductance Power Module for Fast Switching Semiconductors. In *PCIM 2013*, number May, pages 14–16, 2013.

[4] A. J.L. Joannou, D. C. Pentz, J. D. Van Wyk, and A. S. De Beer. Some considerations for miniaturized measurement shunts in high frequency power electronic converters. *2014 16th European Conference on Power Electronics and Applications, EPE-ECCE Europe 2014*, 2014.

[5] Markus Meißner, Jan Schmitz, Felix Weiß, and Steffen Bernet. Current measurement of GaN power devices using a frequency compensated SMD shunt. *PCIM Europe 2019; International Exhibition and Conference for Power Electronics, Intelligent Motion, Renewable Energy and Energy Management*, (May):2045–2052, 2019.

[6] Steve Sandler. Faster-Switching GaN. *IEEE Power Electronics Magazine*, (June):24–31, 2015.

[7] Sayan Seal, Andrea Wallace, Audrey Dearien, Chris Farnell, and Alan Homer Mantooth. A Wire Bondless SiC Switching Cell with a Vertically Integrated Gate Driver, 2020.

[8] Ed Shelton, Nikita Hari, Xueqiang Zhang, Tianqi Zhang, Jin Zhang, and Patrick Palmer. Design and measurement considerations for WBG switching circuits. *2017 19th European Conference on Power Electronics and Applications, EPE 2017 ECCE Europe*, 2017-Janua(1):1–10, 2017.

[9] Luke Shillaber, Li Ran, Yanfeng Shen, and Teng Long. Gigahertz Current Measurement for Wide Band-gap Devices. *ECCE 2020 - IEEE Energy Conversion Congress and Exposition*, (1):2357–2363, 2020.

[10] Jianjing Wang, Mohammad H. Hedayati, Dawei Liu, Salah Eddine Adami, Harry C.P. Dymond, Jeremy J.O. Dalton, and Bernard H. Stark. Infinity Sensor: Temperature Sensing in GaN Power Devices using Peak di/dt. *2018 IEEE Energy Conversion Congress and Exposition, ECCE 2018*, pages 884–890, 2018.

[11] Kangping Wang, Xu Yang, Hongchang Li, Laili Wang, and Praveen Jain. A High-Bandwidth Integrated Current Measurement for Detecting Switching Current of Fast GaN Devices. *IEEE Transactions on Power Electronics*, 33(7):6199–6210, 2018.

[12] Grace Watt, Amy Romero, Rolando Burgos, and Marko Jaksic. Design of a compact, low inductance 1200 v, 6.5 m SiC half-bridge power module with flexible PCB gate loop connection. *Conference Proceedings - IEEE Applied Power Electronics Conference and Exposition - APEC*, 2019-March:2786–2793, 2019.

[13] Zheng Zeng, Jin Wang, Liang Wang, Yue Yu, and Kaihong Ou. Inaccurate Switching Loss Measurement of SiC MOSFET Caused by Probes: Modelization, Characterization, and Validation. *IEEE Transactions on Instrumentation and Measurement*, 70, 2021.

[14] Liqi Zhang, Pengkun Liu, Alex Q Huang, Suxuan Guo, and Ruiyang Yu. An Improved SiC MOSFET-Gate Driver Integrated Power Module with Ultra Low Stray Inductances. *2017 IEEE 5th Workshop on Wide Bandgap Power Devices and Applications (WiPDA)*, pages 342–345, 2017.

[15] Wen Zhang, Zheyu Zhang, and Fred Wang. Review and bandwidth measurement of coaxial shunt resistors for wide-bandgap devices dynamic characterization. *2019 IEEE Energy Conversion Congress and Exposition, ECCE 2019*, pages 3259–3264, 2019.

[16] Wen Zhang, Zheyu Zhang, Fred Wang, Edward V. Brush, and Neil Forcier. High-Bandwidth Low-Inductance Current Shunt for Wide-Bandgap Devices Dynamic Characterization. *IEEE Transactions on Power Electronics*, 36(4):4522–4531, 2021.

Luke Shillaber (S'19) received B.A. and M.Eng. degrees from the University of Cambridge, United Kingdom, in 2018. He is currently working towards a Ph.D. degree at the Department of Engineering, University of Cambridge.

His research interests include high-speed switching of wide-bandgap semiconductors and high bandwidth power measurements.

Yunlei Jiang (S'14) received the B.Sc. degree from Nanjing Normal University, Nanjing, China, in 2015, and the M.Sc. degree from the School of Electrical Engineering, Southeast University, Nanjing, China, in 2018. He is currently working toward the Ph.D. degree with the University of Cambridge, Cambridge, U.K., where he is jointly funded by the Jardine Foundation and Cambridge Trust.

He was a Research Assistant with the Wisconsin Electric Machines and Power Electronics Consortium, University of Wisconsin–Madison, Madison, WI, USA, from 2018 to 2019. He is currently a Jardine Scholar. His research interests include high-performance electrical drive and power electronics. Mr. Jiang wa a recipient of the Outstanding Master's Thesis Award of Jiangsu Province.

Li Ran (Senior Member, IEEE) received the Ph.D. degree in power systems engineering from Chongqing University, Chongqing, China, in 1989. He was a Research Associate with the Universities of Aberdeen, Nottingham, and Heriot-Watt, at Aberdeen, Nottingham, and Edinburgh, U.K., respectively. He became a Lecturer in Power Electronics with Northumbria University, Newcastle upon Tyne, U.K., in 1999, and was seconded to Alstom Power Conversion, Kidsgrove, U.K., from 2001 to 2003. Between 2003 and 2012, he was with Durham University, Durham, U.K., where he was promoted to a Chair in Electrical Power in 2010. He took a sabbatical leave at Massachusetts Institute of Technology, Cambridge, MA, USA, in 2007. Dr Li Ran joined the University of Warwick, Coventry, U.K., as a Professor in Power Electronics - Systems, in 2012. His research interests include the applications of power electronics in electric power generation, delivery, and utilization.

This article has been accepted for publication in IEEE Transactions on Power Electronics. This is the author's version which has not been fully edited and content may change prior to final publication. Citation information: DOI 10.1109/TPEL.2022.3184638

Teng Long (M'13) received the B.Eng. degree from the Huazhong University of Science and Technology, China, the first class B.Eng. (Hons.) degree from the University of Birmingham, UK in 2009, and the Ph.D. degree from the University of Cambridge, UK in 2013. Until 2016, he was a Power Electronics Engineer with the General Electric (GE) Power Conversion business in Rugby, UK. He is currently an Associate Professor with the University of Cambridge. His research interests include power electronics, electrical machines, and machine drives. Dr Long is a Chartered Engineer (CEng) registered with the Engineering Council in the UK.